VIP *Very Important Paper*

Fluorination of Ni-Rich Lithium-Ion Battery Cathode Materials by Fluorine Gas: Chemistry, Characterization, and Electrochemical Performance in Full-cells

Ulf Breddemann[+],[a] Johannes Sicklinger[+],[b] Florian Schipper[+],[c] Victoria Davis,[a] Anna Fischer,[a] Korbinian Huber,[b] Evan M. Erickson,[c] Michael Daub,[a] Anke Hoffmann,[a] Christoph Erk,[d] Boris Markovsky,[c] Doron Aurbach,*[c] Hubert A. Gasteiger,*[b] and Ingo Krossing*[a]

The mild fluorination of Ni-rich NCM CAMs (NCM = nickel-cobalt-manganese oxide; CAM = cathode active material) with a few hundred mbar of elementary fluorine gas (F_2) at room temperature was systematically studied. The resulting fluorinated CAMs were fully analyzed and compared to the pristine ones. Fluorination at room temperature converts part of the soluble basic species on the CAM-surface into a protecting thin and amorphous LiF film. No formation of a metal fluoride other than LiF was detected. SEM images revealed a smoothened CAM surface upon fluorination, possibly due to the LiF film formation. Apparently due to this protecting, but insulating LiF-film, the fluorinated material has a reduced electrical conductivity in comparison to the pristine material. Yet, all fluorinated Ni-rich NCM CAMs showed a considerably higher press density than the pristine material, which in addition increased with higher fluoride concentrations. In addition, fluorination of the Ni-rich CAMs led to the chemically induced formation of small amounts of water, which according to TGA-MS-measurements can be removed by heating the material to 450 °C for a few hours. Overall, the tested fluorinated NCM 811 samples showed improved electrochemical performance over the pristine samples in full-cells with graphite anodes at 30 °C and 45 °C after 500 cycles. Moreover, the fluorination apparently reduces Mn and Co cross talk from the CAM to the anode active material (AAM) through the electrolyte during charge/discharge.

[a] U. Breddemann,[+] V. Davis, A. Fischer, M. Daub, A. Hoffmann, Prof. Dr. I. Krossing
Institut für Anorganische und Analytische Chemie, Cluster of Excellence livMatS, University of Freiburg (VD, AF, IK) and Freiburger Materialforschungszentrum (FMF)
Universität Freiburg
Albertstr. 21, 79104 Freiburg, Germany
E-mail: krossing@uni-freiburg.de
[b] J. Sicklinger,[+] K. Huber, Prof. Dr. H. A. Gasteiger
Chair of Technical Electrochemistry
Technische Universität München
Lichtenbergstrasse 4, 85748 Garching, Germany
E-mail: hubert.gasteiger@tum.de
[c] F. Schipper,[+] E. M. Erickson, B. Markovsky, Prof. Dr. D. Aurbach
Department of Chemistry
Bar-Ilan University
Ramat-Gan 5290002, Israel
E-mail: aurbach@mail.biu.ac.il
[d] C. Erk
BASF SE
Carl-Bosch-Str. 38, 67056 Ludwigshafen, Germany
[+] These authors contributed equally to this work.
    Supporting information for this article is available on the WWW under https://doi.org/10.1002/batt.202000202

1. Introduction

The most traditional cathode active material (CAM) for lithium ion batteries (LIBs) is $LiCoO_2$ (LCO) with a reversible capacity of $\approx 140\ \mathrm{mAh\,g^{-1}}$ and good cycling stability.[1] Yet, cobalt is a critical raw material due to its toxicity and rising cost. Thus, its replacement is one of the driving forces to develop other CAMs for LIBs.[2] LCO has a layered oxide structure in which Co can be substituted with Ni and Mn giving lithium nickel cobalt manganese oxide (NCM) materials with the general composition $Li_{1+w}(Ni_xCo_yMn_z)_{1-w}O_2$ ($x+y+z=1$). Examples include NCM 111 or NCM 523; the three numbers x,y,z present the stoichiometric ratio of Ni:Co:Mn.[3,4,5] To increase the energy density, Li- and Mn-rich NCM materials, often referred to as "overlithiated" NCM or "high-energy NCM (HE-NCM)" were developed.[6] Alternatively, the nickel content may be increased and Ni-rich CAMs such as NCM 622 or NCM 811 are more and more being commercialized due to their higher energy density, lower cobalt concentration, and reduced cost when compared to lithium cobalt oxide (LCO) or NCM 111.[7] NCM 811 and beyond (NCM 851005 or 900505) offer practical capacities up to $\approx 200\ \mathrm{mAh\,g^{-1}}$[8–10] in a layered α-NaFeO$_2$ structure (space group $R\bar{3}m$).[4,8–12] However, the materials have poorer thermal stability and performance at higher temperatures,[7,13] including faster capacity fading and shorter lifetime in comparison to NCM 111.[9,12,14] The high Ni content is challenging:[15] Upon cycling, reactive Ni^{3+} and Ni^{4+} ions form from trace HF (= > moisture

or electrolyte oxidation) on the Ni-rich material surface, degrading battery performance.[16,17] CAMs suffer from increased mechanical strain due to an extended unit cell volume change upon Ni^{2+}/Li^+ cation mixing and structural degradation during cycling including particle cracking.[11,18] Ni-rich NCMs have a more reactive surface compared to e.g. NCM 111,[19] due to an increased basicity leading to a comparatively high (surface) soluble base content (SBC).[20] Thus, the amount of basic Li residuals, including $LiOH \cdot H_2O$ from synthesis and its calcination product Li_2O, on the surface of Ni-rich materials increase with the Ni content.[19] As a consequence, storage of any Ni-rich NCM CAM at higher humidity and/or elevated temperatures modifies the SBC surface layer by H_2O and CO_2 uptake to give LiOH and Li_2CO_3.[21–24] Storing the material at ambient conditions or higher humidity and/or elevated temperatures, leads to the additional development of basic nickel carbonate $NiCO_3 \cdot 2\ Ni(OH)_2 \cdot 4\ H_2O$ (NCBH) as surface impurity.[19,25] By contrast, NCM 111 is not sensitive to SBC surface layer modification even upon storage at 30 °C and 80 % relative humidity for one month or longer.[19,24] Thus, on the surface of the NCM 811 CAM, a comparably high tendency to form these basic surface species in the mixed SBC/NCBH layer during storage is present.[19,21,23–25]

1.1. Surface Modification vs. Bulk Doping[7]

One possibility to stabilize Ni-rich NCM CAMs is surface modification with organic or inorganic surface coatings, e.g., polysiloxane,[26] Li_3PO_4,[27] Al_2O_3,[28] Co_3O_4,[29] TiO_2,[30] ZrO_2,[31] AlF_3,[32,33] polypyrrole,[34] sodium dodecyl sulfate,[35] or carbon.[36] An alternative strategy is cation doping with Mo,[37] Al,[32,38,39] Sn,[39,40] Fe,[39,41] and Zr[42] or even co-doping with several cations.[43] Also fluoride-modification (Review: Ref. [44]) was disclosed in the literature to improve the cycling stability of Ni-rich NCM, e.g., as F^- anion doping from F-sources like $[NH_4]F$, i.e. fluoride[13,45,46] and poly-tetrafluoro-ethylene (PTFE).[7] In addition, treatments e.g. with LiF,[47,48] NiF_2,[48] and $NH_4F \cdot HF$[15] may induce LiF formation on the CAM-surface, but are discussed as coating rather than bulk anion substitution. In any event, this LiF surface modification probably changes the local composition of the electrode-electrolyte interface/-phase and can be beneficial to obtain a better cycling stability, for instance, through a minimization of the electrolyte degradation at its surface.[48] Also, the change of the particle size and the surface of the CAMs when adding LiF to the lithiation step of CAM precursors allows the electrolyte solution to circulate into the microsphere, providing a good contact between the electrode material and the electrolyte.[49] For $NH_4F \cdot HF$,[14] as an example, this was explained by a synergistic stabilizing effect of surface fluorides and formation of rock-salt type NiO in the surface-near region of the oxide particles. In addition, SBC Li-residues, especially Li_2CO_3, were removed during fluoride modification as demonstrated by diffuse-reflectance infrared Fourier transform spectroscopy (DRIFTS) and X-ray photo-electron spectroscopy (XPS). Most likely this was induced

through the acidic intermediate HF produced from heating $NH_4F \cdot HF$.[14]

We have recently reported on a complementary approach to the above-described acid-base or metal-fluoride impregnation methods: oxidative fluorination of CAMs at room temperature with low pressures of pure F_2 gas in a PFA vessel (PFA = perfluoroalkoxy-polymer). Extending from our account on the positive effects upon treating Li- and Mn- rich HE-NCM material with low amounts of F_2 gas,[50] here we oxidatively fluorinated NCM 811 or 851005 CAMs and fully characterized them including full-cell electrochemical cycling experiments of (fluorinated) NCM 811 CAM. To the best of our knowledge, reports using elementary fluorine gas to modify Ni-rich NCM CAMs are hitherto unknown.

Experimental Section

Full experimental details on methods, materials, procedures and measurements are deposited in the Supporting Information (SI). We concentrate here on sections relevant to the discussion and refer the reader to the SI for the rest.

Fluorination of Ni-rich CAMs with F_2 Gas

Ni-rich NCM 811 and NCM 851005 CAMs were obtained from BASF and samples were mildly fluorinated with F_2 gas. Therefore, a Monel Schlenk line of volume 66 mL (SI, Figure S1) was filled with F_2 gas at pressures between 32 to 2200 mbar (or 0.1 to 5.5 mmol). This F_2 volume was expanded into an evacuated transparent 120 mL batch PFA-reactor (SI, Figure S1) containing the CAMs at room temperature (7 g ± 0.04 g; see SI, Figure S2). This process reduces the total pressure in the system to 10 to 800 mbar. Immediately after exposure of the solid CAMs to the fluorine gas, the pressure began to drop, but stabilized within a few minutes, depending on the F_2 amount added. This indicates that the majority of the reaction is over and about 7–8 to 500 mbar pressure is left in the system. To allow for completion of the reaction, the vessel was backfilled with dry nitrogen gas to a total pressure of 1100 mbar. After a total reaction time of 1 hour, the remaining possibly reactive gas was pumped out of the reactor vessel and neutralized in a soda lime tower. The closed setup was transferred into a solvent free dry box, opened, and the fluorinated material was transferred into a storage container until further use.

Li and F Content of the Fluorinated Ni-Rich NCM Materials

To measure the water-soluble lithium (Li) and fluoride (F) concentration of the samples, ion chromatography (IC) studies were carried out for the (non-)fluorinated Ni-rich NCM CAMs. Note that LiF has a low, but reasonable solubility of 1.3 g L^{-1} in water. Thus, 0.2 to 1.0 g fractions of the fluorinated CAMs were eluted with 250 mL ultrapure water, filtered and the fluoride and lithium contents in the filtrate were investigated. As a control, the bulk fluoride concentration of several samples was also verified by analysis after thermal CAM digestion with a fluoride selective electrode (FSE) (Figure 1, SI: Tables S1 and S2 and Figures S3 and S4).
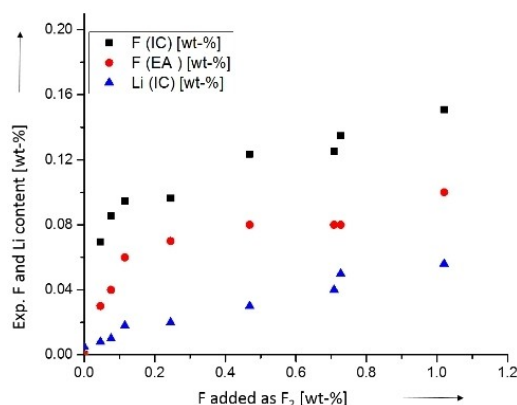
Figure 1. Plots of the fluoride and Li content of the treated NCM 811 CAMs in wt-% as a function of the applied amount of fluorine in wt-%. IC stands for ion chromatography only examining the water-soluble fraction and EA for fluoride selective electrode (FSE) determination investigating the bulk CAMs. The control pristine NCM 811 sample did not contain fluoride.

Full-Cell Battery Measurements

Electrodes were fabricated as described elsewhere.[51] Briefly, 80% (fluorinated) NCM 811 CAM (pristine batch from BASF SE, Germany) was mixed with 5% Super C65 conductive carbon (Imerys, MTI corp. USA), 5% TIMREX KS-6 graphite (Imerys, France) and 10% Solef 5130 polyvinylidenedifluoride (PVDF) binder (Solev5130 from Solvay) in N-methylpyrrolidone (NMP), and cast onto an Al foil (Strem Chemicals Inc., USA) current collector at a loading of ~ 4.3 mg cm^{-2}. Single layer pouch full-cells were fabricated with graphite anodes at a loading of ~ 2.8 mg cm^{-2} with 20% excess capacity (negative to positive electrodes areal capacity ratio of N/P $= 1.2$), using Celgard PP 2500 separators and 350 μL of BASF LP57 electrolyte (1 M LiPF$_6$ ethylene carbonate: ethyl methyl carbonate, 3:7). Areal capacity of the full-cell: ~ 0.7 mAh cm^{-2}, active electrode area: ~ 11.5 cm^2, absolute pouch cell capacity: ~ 8 mAh. The 1 C rate for NCM 811 was set to correspond to 180 mAh g^{-1}. All cells were prepared in triplicate and the results were averaged. Formation procedure for cells: 1 cycle at C/15 followed by 4 cycles at C/10 at 30 °C. For the continuous cycling between 2.0 and 4.2 V, the cells were measured at 30 and 45 °C with a 0.5 C charge and 1 C discharge current and a 30 minutes CV-step at 4.2 V. Every 50 cycles, one cycle was measured during charge and discharge at 0.1 C. Electrochemical impedance spectra were measured using a Solartron battery test unit model 1470 coupled with the frequency response analyzer FRA-1250 from Solartron in the frequency range from 5 mHz to 0.1 MHz with 10 points per decade. Impedance spectra were collected during charge at 4.0 V after formation, 250 and 500 cycles of the continuous cycling test.

ICP-MS Measurements of the Transition metals on the AAM

The graphite electrode from graphite/NCM 811 full-cells was separated from the separator as well as the cathode and freed from electrolyte by washing with DMC. This cleaned graphite electrode was dissolved in hydrochloric acid and filtered. With inductively coupled plasma mass spectrometry (ICP-MS) measurements of the filtrate, the Ni, Co and Mn concentration localized/deposited on the AAM was measured after 500 cycles at 30 °C and 45 °C (Table 2).
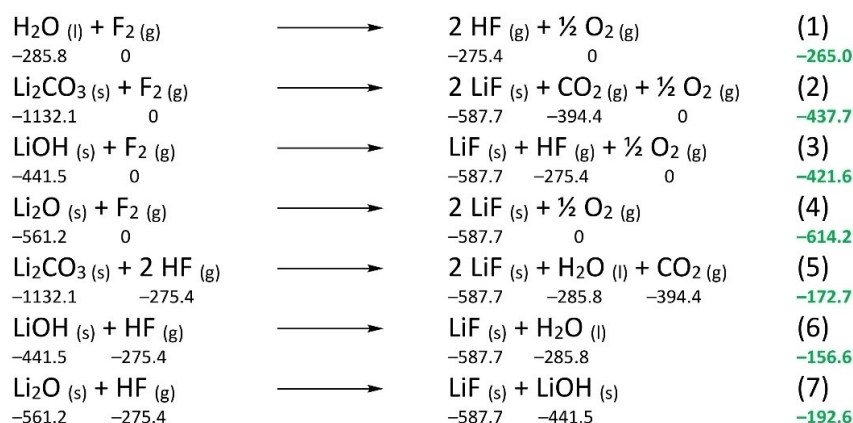
2. Results

Full-cell cycling and impedance measurements of the fluorinated vs. the pristine NCM 811 CAMs revealed considerably improved performance shown below (Figures 9 and 10). To understand this effect, the fluoride-uptake to CAMs, its consequences for structure, properties and morphology are described first, before turning to full-cell cycling and impedance measurements including post mortem analyses and continuing to the discussion section for a comprehensive analysis.
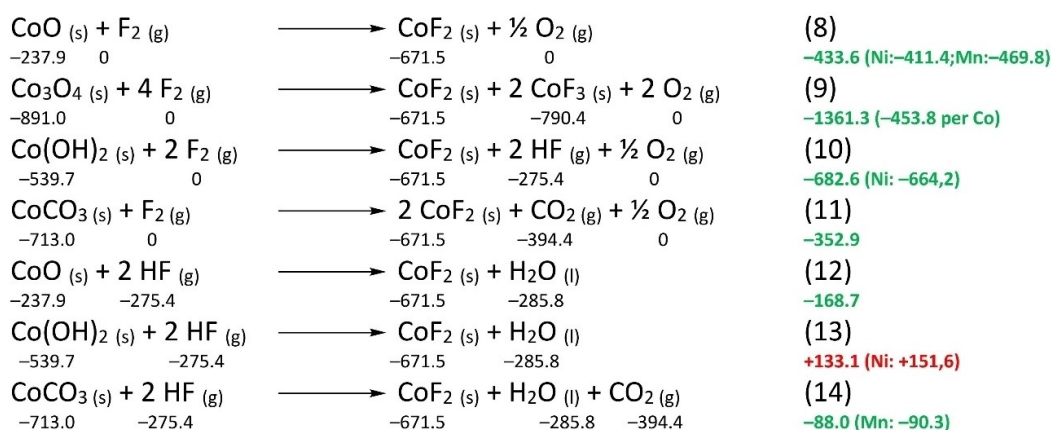
2.1. Li and F Content

To investigate if oxidative fluorination with F$_2$ gas led to fluoride uptake, a series of fluorinated NCM 811 CAMs with theoretically expected F content up to 1 wt.-% were examined in addition to a pristine control sample. The fluoride content of these samples was independently measured by IC as well as FSE and is shown in Figure 1. Note that IC only used aqueous extracts for fluoride determination, while in the FSE approach, the fluoride containing CAMs were thermally digested at 1100 °C in a combustion unit. The resulting hydrogen fluoride was absorbed in a total ionic strength adjustment buffer as absorption solution and determined by means of a fluoride selective electrode. Thus, this method evaluates the total fluoride concentration taken up by the CAM. Since both methods agree reasonably, we suggest that through the aqueous extraction procedure, the full fluoride content of the CAMs is accessible by IC. Turning to the ratio of F added as F$_2$ in comparison to the measured F content: Especially the lower applied F$_2$ amounts up to roughly 0.1 wt.-%F, are taken up by the CAMs more efficiently. From this applied F$_2$ amount on, the system integrates further fluoride at a slower rate. Thus, the reactions targeting at 1 wt.-% F only led to an uptake of about 0.1 to 0.15 wt-% F (Figure 1). The observed lithium concentration measured by IC as a function of the applied gaseous F$_2$ amount runs rather parallel to, but lower than the F-concentrations and also increases with increasing applied F$_2$-amount. IC and FSE measurements behave similar for the (non-)fluorinated NCM 851005 material (SI, Table S2 and Figure S3 & S4).

2.2. Thermodynamics of F$_2$ Gas Reactions with CAM Components

Possibly, several reactions of F$_2$ with the CAM can take place at the same time: the surface SBC layer with compounds such as Li$_2$O, LiOH and Li$_2$CO$_3$ is likely to react with F$_2$, but also the NCBH layer or the layered oxide itself. Based on the thermodynamic data from Ref. [52], we have worked out the possibly underlying standard reaction enthalpies $\Delta_r H^\circ$ in Schemes 1 and 2. Overall, water (adsorbed to the surface of the material) may react with F$_2$ gas to HF and O$_2$ [Eq. (1)]. In addition, the reactions Eqs. (2)–(4) of the SBC constituent's Li$_2$CO$_3$, LiOH and

$$H_2O_{(l)} + F_{2\,(g)} \longrightarrow 2\,HF_{(g)} + \tfrac{1}{2}\,O_{2\,(g)} \qquad (1)$$
$$-285.8 \quad\quad 0 \qquad\qquad\qquad -275.4 \quad\quad 0 \qquad \mathbf{-265.0}$$

$$Li_2CO_{3\,(s)} + F_{2\,(g)} \longrightarrow 2\,LiF_{(s)} + CO_{2\,(g)} + \tfrac{1}{2}\,O_{2\,(g)} \qquad (2)$$
$$-1132.1 \quad\quad 0 \qquad\qquad -587.7 \quad -394.4 \quad\quad 0 \qquad \mathbf{-437.7}$$

$$LiOH_{(s)} + F_{2\,(g)} \longrightarrow LiF_{(s)} + HF_{(g)} + \tfrac{1}{2}\,O_{2\,(g)} \qquad (3)$$
$$-441.5 \quad\quad 0 \qquad\qquad -587.7 \quad -275.4 \quad\quad 0 \qquad \mathbf{-421.6}$$

$$Li_2O_{(s)} + F_{2\,(g)} \longrightarrow 2\,LiF_{(s)} + \tfrac{1}{2}\,O_{2\,(g)} \qquad (4)$$
$$-561.2 \quad\quad 0 \qquad\qquad -587.7 \quad\quad 0 \qquad \mathbf{-614.2}$$

$$Li_2CO_{3\,(s)} + 2\,HF_{(g)} \longrightarrow 2\,LiF_{(s)} + H_2O_{(l)} + CO_{2\,(g)} \qquad (5)$$
$$-1132.1 \quad\quad -275.4 \qquad\qquad -587.7 \quad -285.8 \quad -394.4 \qquad \mathbf{-172.7}$$

$$LiOH_{(s)} + HF_{(g)} \longrightarrow LiF_{(s)} + H_2O_{(l)} \qquad (6)$$
$$-441.5 \quad\quad -275.4 \qquad\qquad -587.7 \quad -285.8 \qquad \mathbf{-156.6}$$

$$Li_2O_{(s)} + HF_{(g)} \longrightarrow LiF_{(s)} + LiOH_{(s)} \qquad (7)$$
$$-561.2 \quad\quad -275.4 \qquad\qquad -587.7 \quad -441.5 \qquad \mathbf{-192.6}$$

Scheme 1. Thermodynamic data to establish the enthalpies of reaction of elementary F_2 gas with H_2O, Li_2CO_3, LiOH, and Li_2O to give LiF, HF, O_2, and CO_2. In addition, reactions of secondarily formed HF [Eqs. (1), (3)] with Li_2CO_3, LiOH and Li_2O to give LiF, H_2O, LiOH, and CO_2 were investigated. Below a substance its enthalpy of formation $\Delta_f H^\circ$ is given in kJ mol^{-1} and at the end, below the equation label, the overall resulting reaction enthalpy $\Delta_r H^\circ$ is given in bold green if exothermic in kJ mol^{-1}.

$$CoO_{(s)} + F_{2\,(g)} \longrightarrow CoF_{2\,(s)} + \tfrac{1}{2}\,O_{2\,(g)} \qquad (8)$$
$$-237.9 \quad\quad 0 \qquad\qquad -671.5 \quad\quad 0 \qquad \mathbf{-433.6\;(Ni:-411.4;Mn:-469.8)}$$

$$Co_3O_{4\,(s)} + 4\,F_{2\,(g)} \longrightarrow CoF_{2\,(s)} + 2\,CoF_{3\,(s)} + 2\,O_{2\,(g)} \qquad (9)$$
$$-891.0 \quad\quad 0 \qquad\qquad -671.5 \quad -790.4 \quad\quad 0 \qquad \mathbf{-1361.3\;(-453.8\;per\;Co)}$$

$$Co(OH)_{2\,(s)} + 2\,F_{2\,(g)} \longrightarrow CoF_{2\,(s)} + 2\,HF_{(g)} + \tfrac{1}{2}\,O_{2\,(g)} \qquad (10)$$
$$-539.7 \quad\quad 0 \qquad\qquad -671.5 \quad -275.4 \quad\quad 0 \qquad \mathbf{-682.6\;(Ni:-664,2)}$$

$$CoCO_{3\,(s)} + F_{2\,(g)} \longrightarrow 2\,CoF_{2\,(s)} + CO_{2\,(g)} + \tfrac{1}{2}\,O_{2\,(g)} \qquad (11)$$
$$-713.0 \quad\quad 0 \qquad\qquad -671.5 \quad -394.4 \quad\quad 0 \qquad \mathbf{-352.9}$$

$$CoO_{(s)} + 2\,HF_{(g)} \longrightarrow CoF_{2\,(s)} + H_2O_{(l)} \qquad (12)$$
$$-237.9 \quad\quad -275.4 \qquad\qquad -671.5 \quad -285.8 \qquad \mathbf{-168.7}$$

$$Co(OH)_{2\,(s)} + 2\,HF_{(g)} \longrightarrow CoF_{2\,(s)} + H_2O_{(l)} \qquad (13)$$
$$-539.7 \quad\quad -275.4 \qquad\qquad -671.5 \quad -285.8 \qquad \color{red}{\mathbf{+133.1\;(Ni:+151,6)}}$$

$$CoCO_{3\,(s)} + 2\,HF_{(g)} \longrightarrow CoF_{2\,(s)} + H_2O_{(l)} + CO_{2\,(g)} \qquad (14)$$
$$-713.0 \quad\quad -275.4 \qquad\qquad -671.5 \quad -285.8 \quad -394.4 \qquad \mathbf{-88.0\;(Mn:-90.3)}$$

Scheme 2. Exemplarily collected thermodynamic data for the reaction of F_2 or intermediately formed HF gas with CoO, Co_3O_4, $Co(OH)_2$, and $CoCO_3$ to give $CoF_{2/3}$ and other plausible products. Below a substance its enthalpy of formation $\Delta_f H^\circ$ is given in kJ mol^{-1} and at the end, below the equation label, the overall resulting reaction enthalpy $\Delta_r H^\circ$ is given in bold green if exothermic and in bold red, if endothermic [in kJ mol^{-1}]. Where available, the data for the respective reaction with Ni- and Mn-compounds are included in parentheses (Ni: XXX; Mn: XXX).

Li_2O with F_2 gas to give LiF, CO_2, O_2 and HF are exothermic (Scheme 1). Scheme 1 also suggests the possible interplay of several follow up reactions, e.g. the intermediately in Eqs. (1) and (3) formed HF could react with the SBC as in Eqs. (5), (6), and (7). Overall, virtually all SBC constituting materials may be transformed on thermodynamic grounds in the exothermic reactions Eqs. (2)–(7) into LiF. It should be noted that also the layered oxide itself or the hydroxide and carbonate ions in $NiCO_3 \cdot 2\,Ni(OH)_2 \cdot 4\,H_2O$ (NCBH)[19,25] could likely react with F_2. However, no complete thermodynamic reference data was found for all thinkable compounds of this material class; the most complete data set is available for the element Co and thus relevant reactions of a representative set of Co-compounds, possibly present within the CAM or its surface, with F_2 and with intermediately formed HF are included in Scheme 2. Where available, the data for the respective reaction with Ni- and Mn-compounds are included in parentheses ($\Delta_f H^\circ$ values in SI).

The reactions included with Scheme 1 and 2 are in agreement with the IC- and FSE-measurements and the above noted pressure drop. The latter agrees with the oxidation of oxide ions being the main reaction as in $F_2 + O^{2-} \rightarrow 2\,F^- + \tfrac{1}{2}\,O_2$. Apparently intermediately formed HF will react further. In addition, carbonates [cf. Eqs. (2), (5), (11) and (14)] cannot be the main partner, as else, pressure would have remained the same or even increased as a consequence of reaction stoichiometry. Yet, it is impossible to assign a preferential oxidation site only based on the thermodynamics. Thus, further analytics was performed.

2.3. Powder X-Ray Diffraction (pXRD)

To elucidate if crystalline metal fluorides were formed, pXRD measurements were carried out for the pristine and the two fluorinated NCM 811 CAMs (Figure 2 and Table 1). pXRD data of both fluorinated samples (F_m: 0.108 wt-% and F_x: 0.126 wt-%)
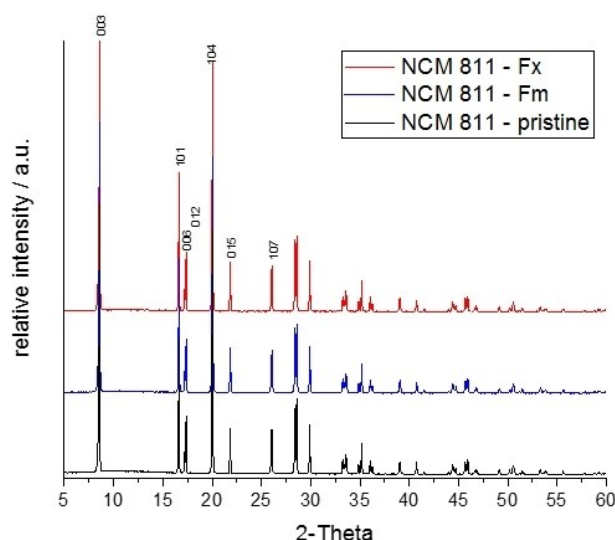
Figure 2. pXRD data of (non-)fluorinated NCM 811 CAM, measured with α Mo$-$K$_{\alpha 1}$ radiation. Miller indices [HKL] assigned to reflexes up to 30° 2θ (F_m: 0.108 wt-% and F_x: 0.126 wt-%) are indicated.

Table 1. pXRD data analysis (Mo$-$K$_{\alpha 1}$ radiation) and STOE fitting of the (non-)fluorinated Ni-rich NCM 811 CAM.

Cell parameters	pristine	0.105 [wt-%] label: F_m	0.126 [wt-%] label: F_x
a [Å]	2.8716(3)	2.87124(23)	2.8719(3)
c [Å]	14.2076(13)	14.2007(11)	14.2035(12)
c/a	4.9476	4.9458	4.9457
V [Å^3]	101.458(13)	101.387(11)	101.454(12)

showed almost identical powder diffractograms and the lattice parameters are within three times the standard deviation identical to that of the rhombohedral cell (space group $R\bar{3}m$) of pristine NCM 811 material (see SI, Figure S5 and Table S3). pXRD measurements of the (non-)fluorinated NCM 851005 showed similar results (see SI, Figure S5 and Table S3). Apparently, all the formed metal fluorides are amorphous. We note that there is no obvious change of the ratios of the relevant peak intensities of the hkl-reflections with the indices 003/104 and [(012)+(006)]/101 for pristine and fluorinated samples and thus no evidence for anion doping (cf. SI, Figures S6 and S7).

2.4. Infrared Spectroscopy (IR)

Classical ATR-IR-spectroscopy of the pristine and fluorinated Ni-rich CAMs showed no changes after exposure to F$_2$ gas – regardless of the applied fluorine concentration. Since LiF is invisible by IR, no direct indication for the formation of any other (bulk) metal fluoride compounds MF$_2$ or MF$_3$ with expected M$-$F (M$\equiv$Ni, Co, Mn) stretches around 600 ± 100 cm^{-1} is evident.[53] All obtained IR spectra appeared to be identical, showing the typical characteristic bands for Ni-rich NCM materials SI, Table S4 & S5 and Figure S8 & S9) and were, therefore, omitted in the main text. However, this might be due

to the low concentration of fluoride containing IR active compounds. Therefore, we switched to surface sensitive DRIFT spectroscopy.

2.5. Diffuse Reflectance Infrared Fourier Transform (DRIFT) Spectroscopy

DRIFT spectroscopy is very sensitive to surface groups on oxide particles and even detects the IR-active species such as CO$_3^{2-}$ and SO$_4^{2-}$ at very low concentrations.[25] To investigate, if IR active M$-$F bonds are present at the surface, DRIFT analyses were carried out for the uncycled NCM 851005 material.[1] However, no terminal M$-$F stretches were evident from the spectra shown in Figure 3. Only the expected and known signatures of surface CO$_3^{2-}$ and SO$_4^{2-}$ are visible.[25]

Only for the highest applied F$_2$ pressure of 2200 mbar (labelled F$_2$ max mbar), the intensity of the carbonate bands is slightly reduced compared to pristine NCM 851005 material. This suggests that Eq. (2), the reaction of F$_2$ with Li$_2$CO$_3$, is of lower importance for the surface chemistry. In addition, the reactions of a transition metal oxide/hydroxide or carbonate collected in Scheme 2 appear not to be prevailing either.
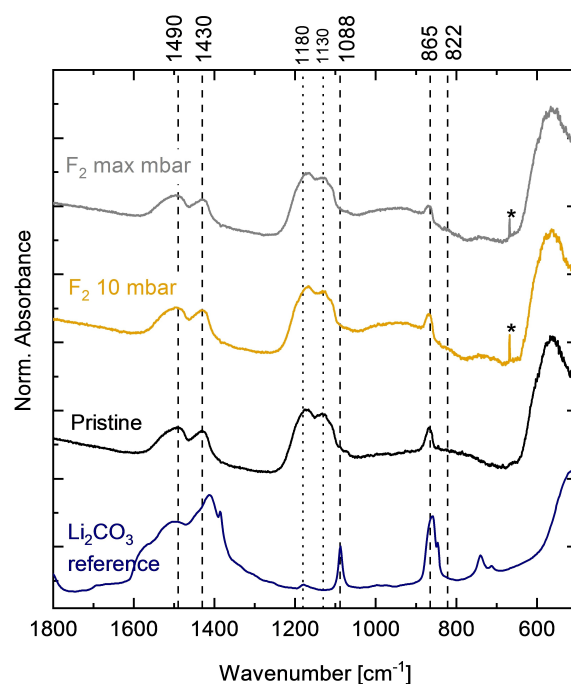

Figure 3. DRIFT spectra of Li$_2$CO$_3$ (reference material), pristine, and two fluorinated NCM 851005 CAMs (F$_2$ 10 mbar $=0.011$ wt-% F and F$_2$ max mbar$=2200$ mbar or 0.24 wt-% F). The bands marked at 1130/1180 cm^{-1} correspond to SO$_4^{2-}$ (from the co-precipitation process of precursor preparation), those at 865 and 1430/1490 cm^{-1} correspond to CO$_3^{2-}$.[25] At the bottom a batch of Li$_2$CO$_3$ is shown as reference. The signals at 670 cm^{-1} marked with an asterisk represent artefacts due to fluctuating amounts of atmospheric CO$_2$ in the spectrometer.

[1] Since we ran out of the pristine NCM 811 material, DRIFT spectroscopy measurements were carried out with the closely related (non-)fluorinated NCM 851005 CAM.

2.6. ⁷Li and ¹⁹F MAS-NMR Studies

Magic angle spinning nuclear magnetic resonance (MAS-NMR) of (non-)fluorinated NCM 811 CAMs were carried out to obtain direct proof for the presence of the in Eqs. (2)–(7) proposed LiF as the most likely metal fluoride in pristine, middle (0.108 wt-% F), and higher (0.126 wt-% F) fluorinated NCM CAMs (Figure 4). The ¹⁹F rotor-synchronized Hahn-Echo MAS NMR spectra of all fluorinated NCM samples show a signal at an isotropic shift of −204.0 ppm that fits very well to the signal of neat solid LiF at −204.5 ppm (SI, Figure S12). There is a second very small signal at −123 ppm originating from traces of PTFE in the samples (probably from the stir bar).

The distortion of the spectra around −100 to −200 ppm results from incomplete subtraction of the background signal originating from the PTFE parts of the MAS probe (SI, Figure S14). In the rotor synchronized solid-echo ⁷Li spectra recorded at 30 kHz MAS, a sharp signal with well resolved spinning sidebands was observed for all samples, fluorinated or not. Its isotropic shift is identical to that of neat LiF at −0.3 ppm, yet it also would match the position[54] in neat Li_2O, Li_2CO_3 or LiOH and thus is rather insensitive to the nature of the counterion (Figure 4; SI, Figure S15 and S16). Additionally, in all the ⁷Li spectra, a very broad signal that does not split into spinning sidebands with a width of about −500 to +1000 ppm is present. It was assigned to the lithium atoms in the bulk of

the Ni-rich material with the highest spatial proximity to the unpaired electrons. Furthermore, it is shifted by more than +300 ppm, if compared to neat LiF, due to the unpaired electron spin density transferred from the neighbored layered Ni-rich NCM oxide to the nucleus (Fermi contact shift). Its linewidth originates from nucleus-electron dipolar interactions as well as a distribution of Fermi contact shifts.[50] The observed chemical shifts in both the ¹⁹F and ⁷Li spectra perfectly match the ones observed for neat LiF and thus were assigned to arise from LiF. However, the spinning sidebands envelope of both, the ⁷Li and ¹⁹F signal, is strikingly broadened in comparison to that of neat LiF (about 150 kHz for ⁷Li and 200 kHz for ¹⁹F, cf. Figures S15 and S16). As the dipole-dipole coupling of ⁷Li and ¹⁹F should be comparable to that in neat LiF and should in general not exceed 100 kHz, the line broadening can only be explained by dipole-dipole interaction of the observed nuclei with the electron spin of the Ni-rich NCM oxide materials. This interaction requests a close spatial proximity. However, since the lines have isotropic shifts identical to neat solid LiF (i.e. no Fermi contact shift is observed), the LiF causing this line is not present within the bulk, but rather coating the Ni-rich NCM material.[50] In addition, ⁷Li and ¹⁹F MAS NMR studies were carried out for the (non-)fluorinated NCM 851005 CAMs and they behave similarly (SI, Figures S15 and S16).

2.7. Scanning Electron Microscopy Measurements

The (non-)fluorinated NCM 851005 CAMs were characterized by scanning electron microscopy (SEM) to study the impact of fluorination on their morphology. The CAMs consist of regular spheroidal particles with a Gaussian distribution of the particle size of around 5–15 μm (Figure 5a, d and g). Pristine material showed an inhomogeneous surface (Figure 5b and c) in comparison to the smoother, more homogenous fluorinated samples (Figure 5e, f, h and i). Yet, overall there is little morphology change upon oxidative fluorination.

2.8. Thermal Stability of Ni-rich NCM CAMs after Fluorination

Thermogravimetric analysis (TGA) and differential thermal analysis (DTA) measurements were carried out at temperatures up to 650 °C by heating with 10 °C min⁻¹ under a flow of nitrogen gas. For the (non-)fluorinated NCM 811 and 851005 CAMs a mass loss between 0.16 to 0.81 % (811) or 0.1 to 1.0 % (851005) was observed by TGA. In addition, DTA measurements revealed no change in thermal stability (SI, Figure S10, Table S11).

2.9. TGA Coupled with Mass Spectrometric Analysis (TGA-MS)

Published TGA-MS measurements of the fluoride containing $LiVPO_4F_{0.45}O_{0.55}$ CAM material[55] showed the release of small amounts of hydrogen fluoride during heating (HF = > m/z = 20). Thus, we investigated this possibility by TGA-MS analysis of
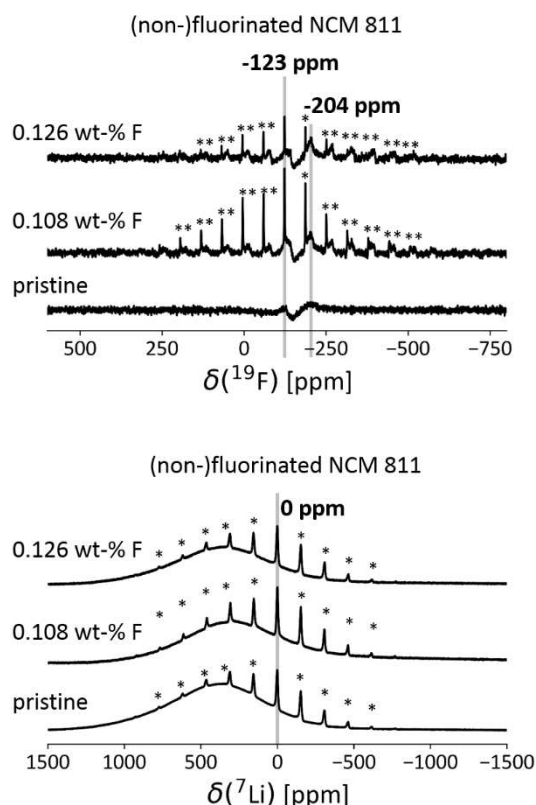

(non-)fluorinated NCM 811

-123 ppm

-204 ppm

0.126 wt-% F

0.108 wt-% F

pristine

500   250   0   −250   −500   −750

$\delta(^{19}F)$ [ppm]

(non-)fluorinated NCM 811

0 ppm

0.126 wt-% F

0.108 wt-% F

pristine

1500   1000   500   0   −500   −1000   −1500

$\delta(^7Li)$ [ppm]

Figure 4. ¹⁹F and ⁷Li MAS NMR studies of pristine, low (0.108 wt-% F) and high (0.126 wt-% F) fluorinated NCM 811 CAMs (lower panel: ⁷Li MAS NMR: 30 kHz spinning; upper panel: ¹⁹F MAS NMR: 30 kHz spinning and ¹⁹F background subtracted for NCM). Spinning sidebands are marked by '*'.
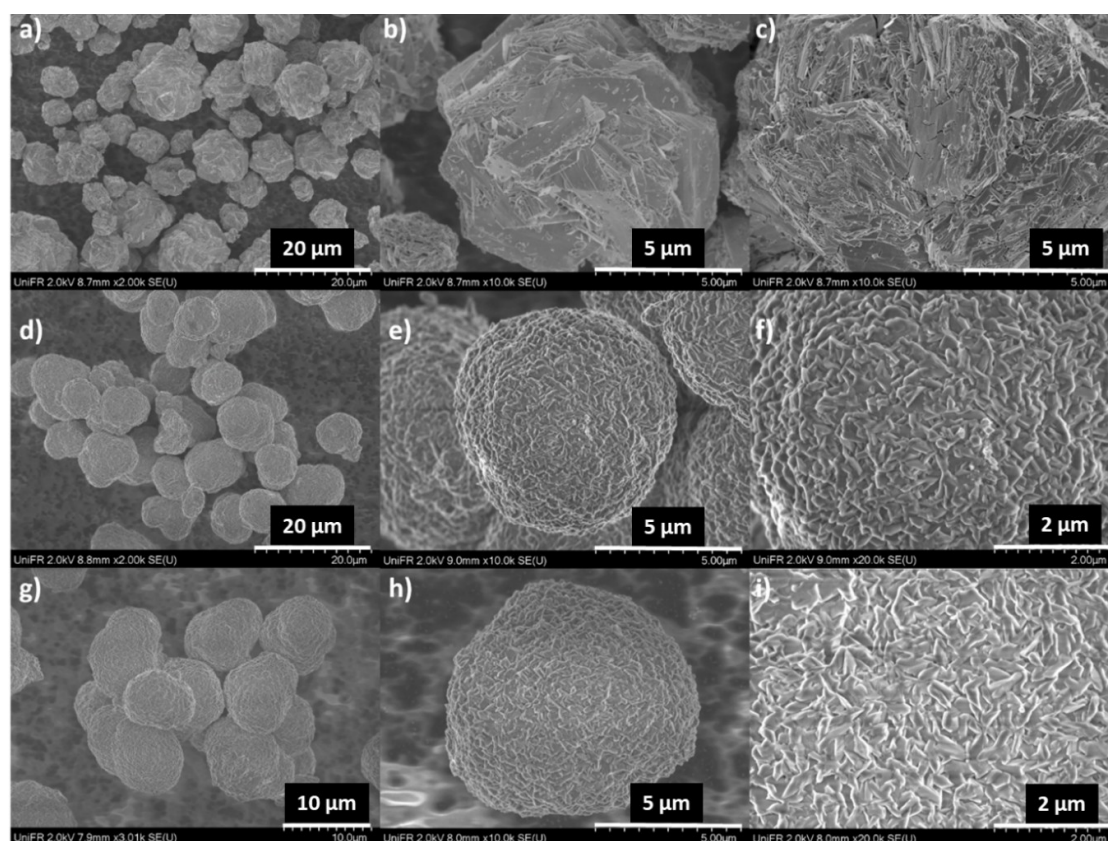
Figure 5. SEM images of pristine NCM 851005 CAM material (a, b, c); CAM with 0.162 wt.-% F (d, e, f); and CAM with 0.240 wt.-% F (g, h, i).

the pristine and two fluorinated NCM 851005 CAMs (0.007 wt-% F and 0.240 wt-% F) to detect any amount of HF, H_2O, O_2 and CO_2 formed during heating the material. TGA-MS measurements in argon were carried out up to 1125 °C for the as received as well as for materials, heated prior in argon to 400 or 450 °C (Figure 6). Due to the loss of absorbed water ($m/z = 18$), the as received material had a mass loss of 0.08 % in the temperature range between 120 and 450 °C (Figure 6A). In agreement with the expectation, the material heated prior to 400 °C had a mass loss of only 0.01 % between 120 and 450 °C (Figure 6D). A significant further mass loss occurs when heating to 1125 °C (adding up to a total mass loss of 7.19 % and 7.30 % for as received and heated material). This is assigned to the bulk decomposition of the material, clearly indicated by the release of O_2 ($m/z = 32$, Figure 6AD). These measurements confirmed the presence of small amounts of water on the surface of the pristine NCM 851005. The fluorinated samples measured without further treatment showed a higher mass loss (0.26 % (0.007 wt-% F)/0.21 % (0.240 wt-% F); Figure 6BE) in comparison to the pristine material (0.08 %; Figure 6A) in the temperature range between 120 and 450 °C. The mass spectra indicate that this increased mass loss is accompanied by the release of little CO_2 ($m/z = 44$) and more H_2O ($m/z = 18$). The total mass loss of these fluorinated samples after heating to 1125 °C is slightly higher compared to the pristine materials (7.48 % (0.007 wt-% F) and 7.42 % (0.240 wt-% F)), due to slightly higher water content (Figure 6BE). Therefore, TGA-MS data confirmed the thermodynam-

ic proposition in Schemes 1 and 2 that the reaction of F_2 gas with Ni-rich NCM finally leads to the formation of water (Figure 6BE). However, TGA-MS gives absolutely no indication for the release of HF ($m/z = 20$). In addition, TGA-MS measurements were taken on the 0.054 wt-% F fluorinated NCM 851005 CAM, untreated or heated to 450 °C after fluorination and prior to TGA-MS analysis (Figure 6CF). The mass loss between 120 and 450 °C was lowered from 0.23 % (Figure 7C, **no** preheating) to 0.05 % (Figure 7F, preheating the fluorinated sample to 450 °C). Thus, fluorinated Ni-rich NCM CAMs should be heated to 450 °C for 5 h prior to use in battery cells, to minimize the amount of water introduced to the system during oxidative fluorination.

2.10. Conductivity Measurements of the Ni-rich CAMs

Conductivity measurements were carried out for the pristine and two fluorinated NCM 811 CAMs. All investigated CAMs show a linear increase of the conductivity in the range of the pressure applied from 2 MPa to 20 MPa (Figure 7). However, in contrast to the samples cited in Refs. [56] and [57–59], the pristine NCM811 material always showed highest conductivities (for the individual values: SI, Table S6 and Figure S17). Furthermore, conductivity measurements were also carried out for the (non-)fluorinated NCM 851005 CAMs and the materials behave similarly (SI, Table S6 and Figure S17).
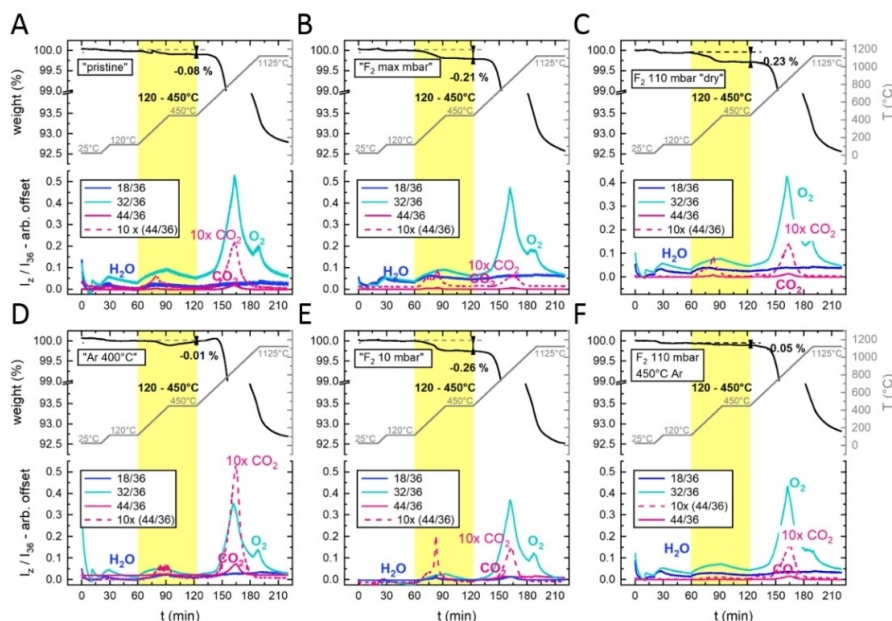
Batteries & Supercaps

Articles
doi.org/10.1002/batt.202000202

Chemistry
Europe
European Chemical
Societies Publishing

Figure 6. TGA-MS measurements of several NCM 851005 CAMs. A) pristine material measured directly. B) Material exposed to 1400 mbar F_2 pressure, labelled "F_2 max mbar" ($=0.24$ wt.-% F). C) Material exposed to 110 mbar F_2 pressure, labelled "F_2 110 mbar (dry)" ($=0.054$ wt-% F). D) pristine material heated to 400 °C in Argon prior to measurement; labelled "Ar 400 °C". E) Material exposed to 10 mbar F_2 pressure, labelled "F_2 10 mbar" ($=0.011$ wt-% F) and F) Material exposed to 110 mbar F_2 pressure and heated to 450 °C in Argon prior to measurement, labelled "F_2 110 mbar, 450 °C Ar)" ($=0.054$ wt-% F). For each sample, the characteristic weight loss (upper half of each panel) and the corresponding mass spectrometric signals (lower half of each panel) are shown for a 10 K min^{-1} temperature ramp from 25 to 1125 °C with isothermal segments at 25, 120, 450 and 1125 °C. The yellow area points out the decomposition temperature of the surface contaminant species LiOH and NCBH.[25] Their decomposition is accompanied by characteristic CO_2 and H_2O fingerprints.
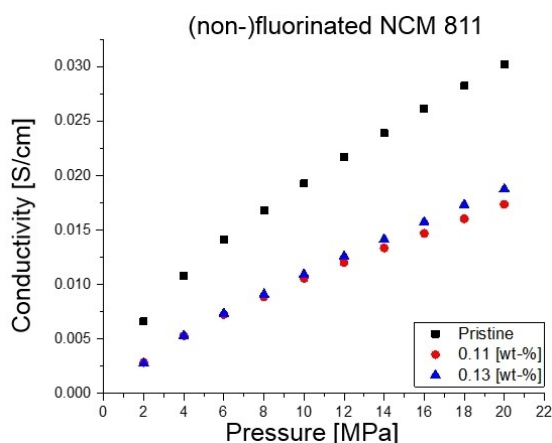

Figure 7. Conductivity measurements of (non-)fluorinated NCM 811 materials.

2.11. Press Density Measurements of the Ni-rich NCM CAMs

Measurements were carried out for the pristine and two fluorinated NCM 811 (Figure 8) and 851005 CAMs. All samples show a linear increase of the density with increasing pressure. Both fluorinated NCM 811 CAMs showed similar press densities that are up to 5% higher than that of the pristine material (for the individual values: SI, Table S7 and Figure S18 for NCM 851005).

2.12. Cycling Behavior of Pristine and Fluorinated Ni-rich NCM 811 CAMs in Full-Cells

The electrochemical performance of the (non-)fluorinated Ni-rich NCM 811 was studied in graphite/NCM 811 pouch full-cells of 8 mAh capacity with LP57 electrolyte. Two different fluoride concentrations, a middle (0.108 wt.-% F) and a higher concentration (0.126 wt-% F) were investigated together with the pristine material. Figure 9 shows the cycling data and the corresponding average charge and discharge voltages measured at 30 °C (left) and 45 °C (right). The middle fluorinated NCM 811 CAMs (0.108 wt-% F, labelled NCM811 Fm in Figure 9) showed for both temperatures the best battery performance after 500 cycles and a clear improvement over the pristine CAM. Still, even the higher fluorinated material (labelled NCM811 Fx) showed for both temperatures an improved stable cycling performance in comparison to the pristine material (Figure 9). At both temperatures, the average charge and discharge voltages calculated from the constant current cycling showed superior results for the middle-fluorinated material NCM811 Fm in comparison to the higher fluorinated NCM811 Fx and the pristine NCM811 materials. The higher fluorinated and pristine materials have rather similar average charge and discharge voltages at 30 °C. However, at 45 °C they differ visibly during discharge and even the higher fluorinated material showed a slower decrease of the average discharge voltage and a lower voltage hysteresis upon cycling compared to the pristine material (Figure 9). Yet, best performance was achieved for the middle-fluorinated material containing 0.108 wt-% F.
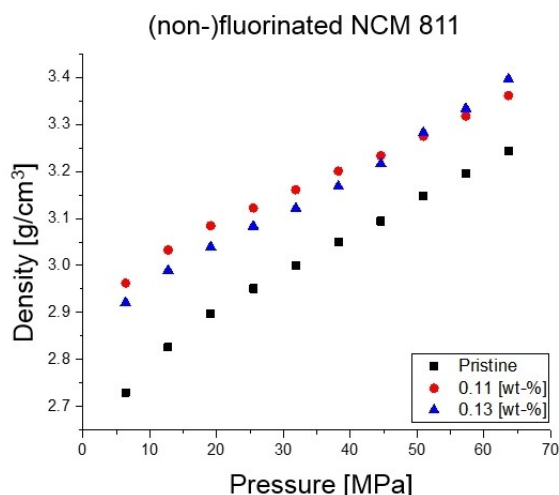
Figure 8. Press density measurements of (non-)fluorinated NCM 811.

2.13. Impedance Measurements

Figure 10 shows Nyquist plots of electrodes including (non-)fluorinated NCM 811 CAMs after 250 cycles (closed symbols) and after 500 cycles (open symbols) at 30 °C (Figure 10a) and 45 °C (Figure 10b), measured during charge at 4.0 V from 5 mHz to 0.1 MHz. In agreement with the improved cycling behavior, the middle-fluorinated material NCM 811 Fm showed for both

temperatures the lowest surface film resistance throughout cycling. The higher fluorinated NCM 811 Fx and pristine NCM 811 CAMs had similar, but considerably higher values for both temperatures. In Fig 10c, the resistances calculated from the middle-to-low frequency semicircles are plotted against the number of cycles; they were fitted with Z-view. Again, the middle-fluorinated material NCM 811 Fm showed for both temperatures the best values and the higher fluorinated NCM 811 Fx as well as the pristine NCM 811 CAMs showed similar, but inferior values for both temperatures, with slightly lower resistance for the higher fluorinated CAM.

2.14. Transition Metal Leaching from the CAM and Migration to the Anode Active Material (AAM)

The dissolution of transition metals from the CAM into the electrolyte solution upon prolonged cycling with possible deposition on the AAM is detrimental to battery performance.[5,60] To investigate the effect of oxidative fluorination on the metal leaching, cells with pristine and fluorinated (0.108 wt-% F and 0.126 wt-% F) NCM 811 were disassembled after 500 cycles and the nickel, cobalt, and manganese concentration localized/deposited on the AAM after 500 cycles at 30 °C and 45 °C was determined by ICP-MS (Table 2).

Apparently, the Ni leaching is little affected by the fluorination. However, the ICP-MS measurements showed the
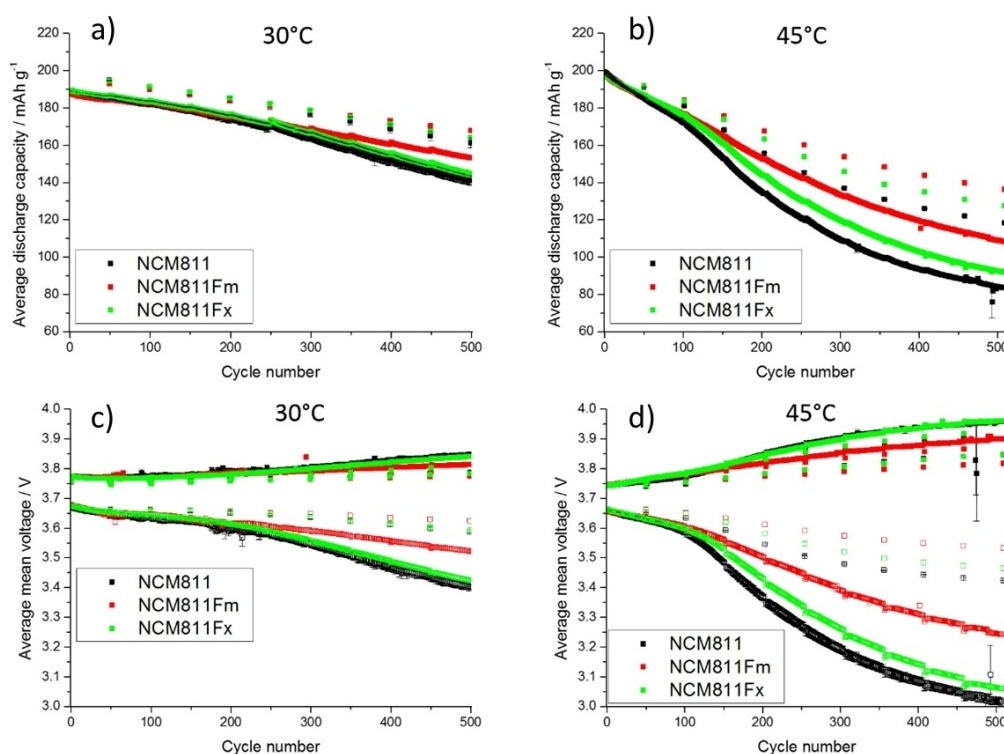

Figure 9. Full-cell cycling data (triplicate measurements including the standard deviation as error bars) of the (non-)fluorinated NCM 811 CAMs measured in full-cells at 30 °C (a, left) and 45 °C (b, right) with LP57 electrolyte. Fm stands for 0.108 wt-% F and Fx for 0.126 wt-% F. For the continuous cycling between 2.0 and 4.2 V and after the five formation cycles (omitted), the cells were measured with a 0.5 C charge and 1 C discharge current and a 30 minutes CV-step at 4.2 V. Every 50 cycles, one cycle was measured at 0.1 C for charge and discharge. c, d) Average charge and discharge voltages upon cycling, omitting the first five formation cycles, as shown in (a, b). Fm stands for 0.108 wt-% F and Fx for 0.126 wt-% F.
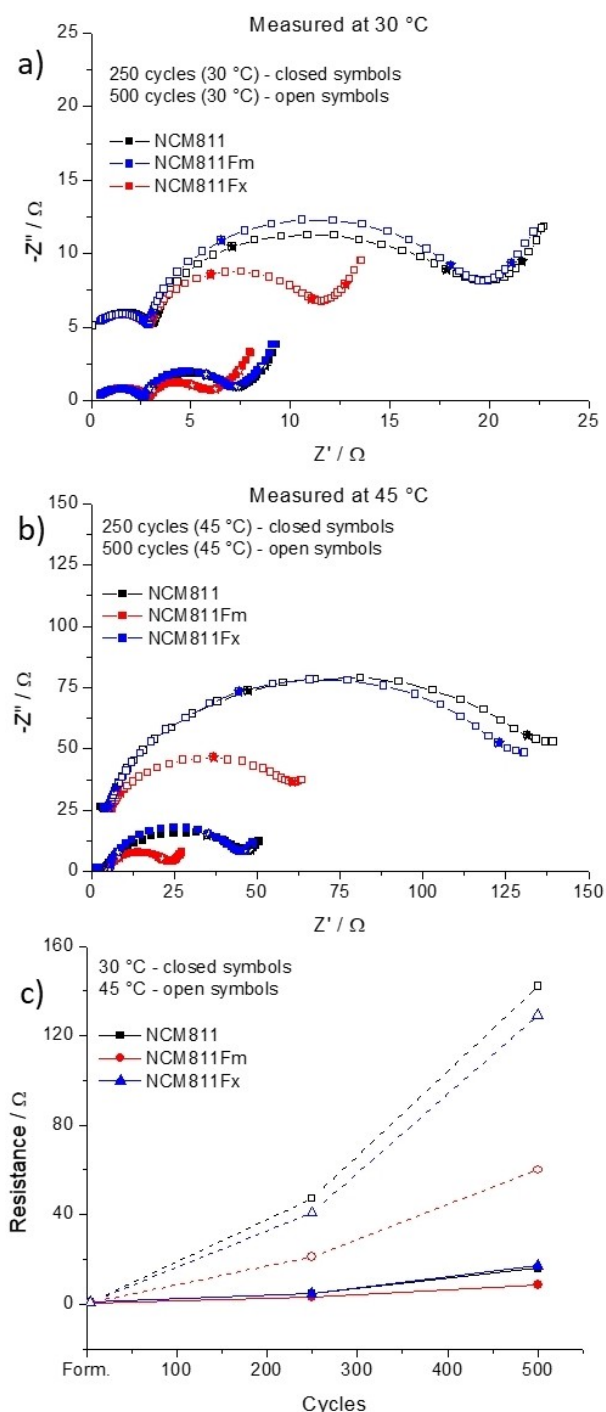
Figure 10. Nyquist plots of cells comprising (non-)fluorinated NCM 811 CAMs after 250 cycles (closed symbol) and 500 cycles (open symbol) at 30 °C (a) and 45 °C (b). Fm stands for 0.108 wt-% F and Fx for 0.126 wt-% F. For each of the plots, the impedance at 500 cycles was offset in the imaginary impedance by −5 ohms at 30 °C, and −25 ohms at 45 °C. The results have not been normalized by multiplying the geometric area of the electrode or the loading. Yet, the comparison is valid, since the electrode loading, as well as their geometric and electrochemical surface area were the same between each of the 6 cells. Impedance measured at 10, 1, 0.1 and 0.01 Hz is indicated by stars. The resistance measured from the middle-to-low frequency semi-circles are plotted against cycles, fitted with Z-view (c).

highest concentrations of Co and Mn in AAMs dissolved from the pristine material. The cells with the middle and higher

fluorinated CAMs, showed a large reduction of the leaching to about one-half of the pristine (for Co), or even to one-third of the pristine materials (Mn at 45 °C). Thus, the fluorination apparently reduces transition metal cross talk for Co and Mn from the CAM to the AAM through the electrolyte solution.

3. Discussion

Earlier work showed that exposure of CAMs to higher F_2 pressures at elevated temperatures only diminished[50] subsequent discharge capacities in battery cycling.[61] This capacity reduction is in agreement with an oxidation of the transition metal octahedral network, delithiation, and formation of larger amounts of amorphous LiF according to Eq. (15).

$$Li[MO_2] + x(^1/_2\ F_2) \rightarrow Li_{1-x}[MO_2] + x\ LiF$$
$$(M{=}Co,\ Ni,\ Mn) \tag{15}$$
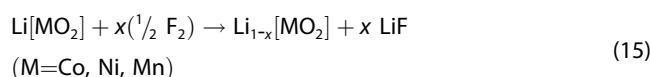
Therefore, we concentrated here on the effect of mild room temperature (surface) fluorination of Ni-rich NCM material. Our main idea was to convert the SBC, i.e. Li_2O, LiOH, Li_2CO_3 and eventually the NCBH surface phase[18–23] into harmless phases for the electrochemical performance in full-cells.

3.1. Effects of Fluorine Gas Treatments on the Electrochemical Performance of Ni-rich NCM 811

Both fluorinated samples showed enhanced electrochemical performance after 500 cycles at 30 °C and 45 °C, and a clear improvement over the pristine CAM (Figure 9). At both temperatures, the middle-fluorinated sample (0.108 wt.-% F) showed superior battery performance, more stable average charge/discharge voltages, and the lowest surface film resistance throughout cycling (at 250 and 500 cycles). In the following, we attempt to rationalize these observations.

3.2. Reduction of the SBC Content by Fluorination

Apparently, the room temperature reaction with low F_2 pressures produces a thin LiF layer on the CAM. This agrees with the thermodynamics of the reactions shown in Scheme 1, Eqs. (2)–(7) as well as the direct observation of LiF in the MAS-NMR. Yet, the DRIFT spectra showed that the Li_2CO_3 surface content is only slightly diminished. Support comes from thermodynamics: the reaction of Li_2CO_3 with F_2 [Eq. (2)] is by 176 kJ mol^{-1} **less favored** in $\Delta_r H^\circ$ than Eq. (4), the reaction of F_2 with Li_2O. Therefore, Eq. (4) could be the major oxidative fluorination path. In addition, this fits with the observed pressure drop after fluorination: in Eq. (4), one equivalent F_2 gas only releases half an equivalent O_2 gas. Since the fluorine molecule F_2 is gaseous and very small, this gas molecule can in principle reach every pore of a solid structure. Advantageously, it was expanded within seconds to the evacuated reactor vessel with the porous CAM. Thus, despite its high reactivity, we

Table 2. Results of ICP-MS measurements of the hydrochloric acid extracts to determine the nickel, cobalt, and manganese concentration in wt-% localized on the AAM after 500 cycles at 30 °C or 45 °C and dissolution of metals in hydrochloric acid.

NCM 811 CAM	Ni [%] at 30 °C	Co [%] at 30 °C	Mn [%] at 30 °C	Ni [%] at 45 °C	Co [%] at 45 °C	Mn [% at 45 °C
pristine	0.067	0.052	0.259	0.076	0.062	0.617
0.108 wt-% F	0.073	0.029	0.152	0.065	0.032	0.178
0.126 wt-% F	0.058	0.025	0.144	0.065	0.031	0.209

expect that it did immerse into every pore of the material. Already earlier work[50,62] showed that thin LiF surface films on CAMs have positive effects on the performance of the battery. The transformation of parts of the surface accessible basic compounds into chemically neutral and in the electrolyte solution insoluble LiF presumably reduced the SBC and thereby led to less degradation of the electrolyte during cycling resulting in reduced impedance built-up.

3.3. Limited Fluoride Uptake

For the screening fluorination reactions performed, the fluoride content of the nickel-rich NCM CAMs after room temperature oxidative fluorination was always lower than 0.25 wt-% F, although gas pressures targeting up to an ideal fluoride uptake of up to 1.0 wt.-% (NCM 811) and for NCM 851005 even up to 3.0 wt.-% were applied (Figure 1; Figure S3, Table S1). Thus, a certain amount of self-levelling of the fluoride uptake by oxidative fluorination appears to occur. This may be induced by the action of the protecting LiF layer, which is inert towards further oxidation with F_2.

3.4. How Does Fluorination Reduce Co and Mn Leaching from the CAM?

The transition metal dissolution from closely related pristine NCM 622 and their migration to the graphite anode was earlier investigated: at high potentials Ni, Mn, and Co dissolved in the electrolyte and deposited nearly stoichiometrically on the AAM.[17] Our ICP-MS measurements of the Ni, Co and Mn concentration on the graphite AAM after 500 cycles at 30 °C and 45 °C (Table 2) indicate that Ni leaching is slightly reduced by fluorination. By contrast, a large leaching-reduction to about one-half of the pristine (for Co), or even to one-third of the pristine materials (Mn at 45 °C) was observed. We discuss some background first before turning to this observation.

3.5. On the Oxidation State of TMs in NCM CAMs

Recent analyses showed that in pristine discharged NCM CAMs the Ni ions are present in three different oxidation states, mainly 2+, but also 3+, and 4+. Co ions adopt the 3+ oxidation state and Mn ions exist as 4+.[63] The amount of Ni^{3+} ions increases with increasing Ni content in NCMs, while that of Ni^{2+} ion decreases. Ni^{4+} is only found in Ni-rich NCM CAMs such as NCM 811.[63] The valence state of the redox ions

present[25,64] depends on the charge state/composition and follows for $Li_{1-x}Ni_{1/3}Co_{1/3}Mn_{1/3}O_2$ the amount of x present: Ni^{2+}/Ni^{3+} for $0 \leq x \leq 1/3$, Ni^{3+}/Ni^{4+} for $1/3 \leq x \leq 2/3$, and Co^{3+}/Co^{4+} for $2/3 \leq \times 1$.[65]

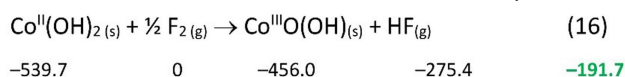### 3.6. Structural Instability Induced by the Jahn-Teller Effect

Both LCO and NCM CAMs have a layered structure, in which the metal atoms are octahedrally coordinated by oxygen atoms and the lithium ions are localized in-between the MO_6 layer (M≡Ni, Co, and Mn).[66] In such an environment, the d-orbitals of the transition metals are split into an e_g set (d_{x2-y2}; d_{z2}) and a t_{2g} set (d_{xy}; d_{xz}; d_{yz}). The Jahn-Teller-(JT-)effect describes a further splitting of the d-orbitals with a d^{4-9} configuration to remove degeneracies. This leads either to *compressed* or *elongated* structures (both with local D_{4h} symmetry). Hence, the JT-effect can produce structural instabilities in the CAM during charge and discharge, which may lead to the preferential dissolution of the lattice metal JT-ion into the electrolyte, facilitated by traces of HF in the electrolyte.[67] Ions with strong JT-effect are those, in which the degenerate e_g set is unevenly distributed, i.e. d^4 high spin (Mn^{3+}) and d^7 low spin (Co^{2+}; Ni^{3+}). Thus, it is expected that ions in these configurations will, due to the structural JT-instability, more easily leach into the electrolyte and finally deposit on the AAM.

Yet, the presence of accessible, presumably surface bound Co^{2+} as well as Mn^{3+} is against the conventional wisdom (see above). However, support for this hypothesis comes from the investigation[68] of the related $Na_{2/3}Co_{2/3}Mn_{1/3}O_2$ prepared by a coprecipitation method. The sodium intercalation in P2–$Na_{2/3}Co_{2/3}Mn_{1/3}O_2$ was investigated by X-ray absorption spectroscopy (XAS). The oxidation states in pristine $Na_{2/3}Co_{2/3}Mn_{1/3}O_2$ were assigned as Co^{3+} and Mn^{4+}. Important features of Co^{2+} and Mn^{3+}, for example, energy shifts and bond distances, were observed using XAS and indicate that both redox couples Co^{3+}/Co^{2+} and Mn^{4+}/Mn^{3+} are to some extent simultaneously present in the discharged state.[68] Therefore, we suggest that also in the Ni-rich $Li_{1+w}(Ni_xCo_yMn_z)_{1-w}O_2$ phases some of the cobalt could exist in the divalent state together with reduced Mn^{3+}.

3.7. Effect of Oxidative Fluorination on Co and Mn Leaching

In the pristine NCM 811 CAM used in this study, the leaching of all three metals, potentially as the JT-ions Mn^{3+}, Co^{2+} and Ni^{3+} with structural instability, is similar. Upon fluorination, the Ni leaching is only slightly diminished. The reason could be that

Batteries & Supercaps

Articles
doi.org/10.1002/batt.202000202

Chemistry Europe
European Chemical
Societies Publishing

Ni^{3+} is the "natural" oxidation state of Ni in the discharged NCM CAM and more difficult to oxidize than the JT-ions with lower oxidation state (Co^{2+}) or the easier to oxidize Mn^{3+}. Thus, low oxidation state surface Co^{2+} and Mn^{3+} ions present in the pristine material could, in addition to SBC, be preferentially oxidized by the gaseous reagent F_2 to the non-leachable Co^{3+}/Mn^{4+} ions that are immediately covered by a concomitantly formed LiF surface film insoluble in the electrolyte. Apparently, this does not lead to Co–F or Mn–F bond formation (cf. DRIFTS), but rather would include for example the exothermic oxidation of surface $Co^{II}(OH)_2$ to $Co^{III}O(OH)$ as in Eq. (16),

$$Co^{II}(OH)_{2\,(s)} + \tfrac{1}{2}\,F_{2\,(g)} \rightarrow Co^{III}O(OH)_{(s)} + HF_{(g)} \qquad (16)$$

−539.7	0	−456.0	−275.4	**−191.7**

delivering HF, which immediately reacts further with other basic surface sites according to Schemes 1 and 2. Eq. (16) is exothermic by $-191.7\ kJ\,mol^{-1}$ (bold **green**; $\Delta_f H^\circ$ of all components[52,69] is given below the substances). $Co^{III}O(OH)$ formation is already induced by oxygen in alkaline solution,[70] and thus appears sensible to work with F_2 as oxidant. Mn^{3+} would similarly be converted according to Eq. (15) with M≡Mn to MnO_2. Thus, the amount of redox accessible low oxidation state surface Co^{2+} and Mn^{3+} ions susceptible to leaching could be lowered by the oxidative gas phase fluorination. Consequently, Co and Mn leaching would be strongly diminished, but Ni leaching is little changed. However, all ions are slightly protected from leaching by formation of an amorphous and protecting LiF surface film. This would also account for the slight reduction of Ni leaching observed in 3 out of 4 cases for the fluorinated NCM 811 CAMs (Table 2).

3.8. Secondary Effects of Fluorination

3.8.1. Formation of Trace Water

TGA-MS analysis showed for the fluorinated samples slightly higher mass loss in comparison to the pristine material in the temperature range between 120 °C and 450 °C. This agrees with the chemical formation of water as a consequence of the fluorination as given in Eq. 5 and 6 in Scheme 1. pXRD data showed a tiny influence of the fluorination on the unit cell parameters, in which the pristine material had the smallest unit cell (Figure S7, Table S3). This might be consistent with the incorporation of H_2O in the material during the reaction of fluorine gas with the Ni-rich NCM CAMs. However, heating for a few hours at 450 °C did remove these small water amounts effectively according to the TGA-MS analysis. In agreement, the material, heated to 450 °C for 5 h had the smallest unit cell of all samples. Thus, for an improved battery performance, an intermediate drying step at 450 °C is recommended, if CAMs exposed to oxidative fluorination are to be used in LIBs.

3.8.2. Reduced Conductivity, but Increased Press Density

Electronic conductivities of CAMs measured with a four-point conductivity test method may increase upon fluoride uptake, i.e. the conductivity of vanadium phosphates improved from $Li_3V_2(PO_4)_3$ ($3.7\times10^{-7}\ S\,cm^{-1}$) over fluorinated $Li_3V_2(PO_4)_{2.95}F_{0.05}$ ($1.2\times10^{-6}\ S\,cm^{-1}$) to $Li_3V_2(PO_4)_{2.90}F_{010}$ ($7.2\times10^{-6}\ S\,cm^{-1}$), but again decreased for highest F-content in $Li_3V_2(PO_4)_{2.85}F_{0.15}$ ($9.2\times10^{-7}\ S\,cm^{-1}$).[56] Similarly, fluorinated lithium iron fluorophosphates have a higher conductivity (LiFePO$_4$F: $\approx1\times10^{-7}\ S\,cm^{-1}$ at 300 K) than non-fluorinated $LiFePO_4$ ($\approx1\times10^{-9}\ S\,cm^{-1}$ at 300 K).[57–59] However, in our case the conductivities decreased, but instead the press densities increased. To account for this observation, one should note that typically inorganic fluorides such as LiF do act as fluxing reagents. Thus, LiF is most widely used as a flux in the production of ceramics, such as enamels, glasses and glazes. The pXRD analyses of our fluorinated Ni-rich CAMs showed that the LiF formed is probably amorphous. In addition, SEM-images showed for the non-treated material a rougher surface in comparison to both fluorinated samples with smoothened surfaces. Apparently, this – possibly through the amorphous character improved – fluxing property of the homogeneous LiF-surface may facilitate sintering and increases densities of the fluorinated CAM powders upon pressurization. The rough trend is that higher fluoride concentrations led to higher press densities. This might be related to the reduction of the SBC layer by fluorination to give LiF. However, LiF is an electrical insulator and therefore fluorinated NCM 811 (and also NCM 851005) has a reduced conductivity in comparison to the pristine material.

4. Conclusions

The treatment of Ni-rich NCM CAM with low pressures (a few hundred mbar) of fluorine gas at room temperature lowers the SBC concentration on the surface of the material, producing a thin LiF film. DRIFT spectra suggest that the main reaction partner within the SBC is Li_2O and the less favored reaction of F_2 with Li_2CO_3 only occurs to a small degree. In addition, no formation of metal fluorides other than LiF was detected. SEM images revealed a smooth coating of the fluorinated CAM particles, possibly due to a LiF film. This X-ray amorphous LiF film may have a fluxing property and, favorably, all fluorinated Ni-rich NCM CAMs showed a considerably higher press density than the pristine material. However, apparently due to this insulating LiF-film, the fluorinated material has a reduced conductivity in comparison to the pristine one. As a co-product, fluorination of the Ni-rich CAM leads to the chemical formation of small amounts of water, which according to TG-MS-measurements can be removed by heating the material to 450 °C for a few hours. Overall, the tested fluorinated NCM 811 samples showed enhanced electrochemical performance in full-cells at 30 °C as well as 45 °C after 500 cycles and a clear improvement over the pristine NCM 811 CAM. At both temperatures, the middle-fluorinated sample (0.108 wt-% F) showed the superior battery performance, much more stable average charge and

Batteries & Supercaps

Articles
doi.org/10.1002/batt.202000202

Chemistry
Europe
European Chemical
Societies Publishing

discharge voltages and the lowest built-up of surface film resistance after 250 and 500 cycles. These improvements may result from diminished electrolyte decomposition during cycling leading to reduced impedance built-up. Possibly, this reduction is induced by reduction of the SBC content and formation of the protecting thin amorphous surface LiF-film. Further improving the electrochemical performance, Mn and Co leaching from the CAM and their subsequent deposition on the AAM is reduced after 500 cycles at 30 °C and 45 °C. While the Ni dissolution is almost unaffected, the cells with the fluorinated CAMs showed a large leaching-reduction to about one-half of the pristine (Co), or even to one-third of the pristine materials (Mn at 45 °C). Thus, the fluorination apparently reduces Co and Mn cross talk from the CAM to the AAM through the electrolyte solution during charge/discharge. This may tentatively be assigned to the oxidative fluorination, which suppresses the preferential leaching of the surface bound strong Jahn-Teller ions Co^{2+} (d^7) and Mn^{3+} (d^4) in the pristine material by oxidizing them to non-leachable Co^{3+} (e.g., as CoO(OH)) and Mn^{4+} (e.g., as MnO_2) imbedded into the protecting and insoluble surface LiF film on the CAM.

Acknowledgements

Conflict of Interest

The authors declare no conflict of interest.

Keywords: Lithium-ion batteries · Ni-rich cathode materials · mild surface fluorination · fluorine gas · electrochemical testing.

[1] a) V. Etacheri, R. Marom, R. Elazari, G. Salitra, D. Aurbach, *Energy Environ. Sci.* **2011**, *4*, 3243; b) J. B. Goodenough, Y. Kim, *Chem. Mater.* **2010**, *22*, 587; c) U. Kasavajjula, C. Wang, A. J. Appleby, *J. Power Sources* **2007**, *163*, 1003; d) M. Winter, J. O. Besenhard, *Solid-State Electron.* **1999**, *45*, 31; e) P. N. Kumta, D. Gallet, A. Waghray, G. E. Blomgren, M. P. Setter, *J. Power Sources* **1998**, *72*, 91.

[2] L. Leyssens, B. Vinck, C. van der Straeten, F. Wuyts, L. Maes, *Toxicology* **2017**, *387*, 43.

[3] a) Y.-H. Cho, D. Jang, J. Yoon, H. Kim, T. K. Ahn, K.-W. Nam, Y.-E. Sung, W.-S. Kim, Y.-S. Lee, X.-Q. Yang, et al., *J. Alloys Compd.* **2013**, *562*, 219; b) P. Hou, X. Wang, D. Song, X. Shi, L. Zhang, J. Guo, J. Zhang, *J. Power Sources* **2014**, *265*, 174; c) K. Wu, F. Wang, L. Gao, M.-R. Li, L. Xiao, L. Zhao, S. Hu, X. Wang, Z. Xu, Q. Wu, *Solid-State Electron.* **2012**, *75*, 393; d) C.-C. Yang, Z.-Y. Lian, S. J. Lin, J.-Y. Shih, W.-H. Chen, *Solid-State Electron.* **2014**, *134*, 258; e) H. Kaneda, *Int. J. Electrochem. Sci.* **2017**, 4640; f) S. Li, X. Fu, J. Zhou, Y. Han, P. Qi, X. Gao, X. Feng, B. Wang, *J. Mater. Chem. A* **2016**, *4*, 5823; g) R. Koerver, I. Aygün, T. Leichtweiß, C. Dietrich, W. Zhang, J. O. Binder, P. Hartmann, W. G. Zeier, J. Janek, *Chem. Mater.* **2017**, *29*, 5574; h) F. Schipper, M. Dixit, D. Kovacheva, M. Talianker, O. Haik, J. Grinblat, E. M. Erickson, C. Ghanty, D. T. Major, B. Markovsky, et al., *J. Mater. Chem. A* **2016**, *4*, 16073; i) D.-C. Li, T. Muta, L.-Q. Zhang, M. Yoshio, H. Noguchi, *J. Power Sources* **2004**, *132*, 150; j) J. Oh, J. Kim, Y. M. Lee, D. O. Shin, J. Y. Kim, Y.-G. Lee, K. M. Kim, *Mater. Chem. Phys.* **2019**, *222*, 1; k) Y. Sun, Z. Zhang, H. Li, T. Yang, H. Zhang, X. Shi, D. Song, L. Zhang, *Dalton Trans.* **2018**, *47*, 16651; l) B.-J. Chae, J. H. Park, H. J. Song, S. H. Jang, K. Jung, Y. D. Park, T. Yim, *Solid-State Electron.* **2018**, *290*, 465; m) G. Li, L. Qi, P. Xiao, Y. Yu, X. Chen, W. Yang, *Solid-State Electron.* **2018**, *270*, 319; n) M. A. Mezaal, L. Qu, G. Li, W. Liu, X. Zhao, K. Zhang, R. Zhang, L. Lei, *Solid-State Electron.* **2017**, *21*, 145.

[4] Y. Xi, Y. Liu, D. Zhang, S. Jin, R. Zhang, M. Jin, *Solid State Ionics* **2018**, *327*, 27.

[5] M. Evertz, F. Horsthemke, J. Kasnatscheew, M. Börner, M. Winter, S. Nowak, *J. Power Sources* **2016**, *329*, 364.

[6] a) E. M. Erickson, F. Schipper, T. R. Penki, J.-Y. Shin, C. Erk, F.-F. Chesneau, B. Markovsky, D. Aurbach, *J. Electrochem. Soc.* **2017**, *164*, A6341–A6348; b) E. M. Erickson, C. Ghanty, D. Aurbach, *J. Phys. Chem. Lett.* **2014**, *5*, 3313; c) P. Rozier, J. M. Tarascon, *J. Electrochem. Soc.* **2015**, *162*, A2490–A2499; d) V. A. Godbole, J.-F. Colin, P. Novák, *J. Electrochem. Soc.* **2011**, *158*, A1005; e) C. Villevieille, J. L. Gomez-Camer, M. Hess, P. Novak, *J. Electrochem. Soc.* **2014**, *161*, A871–A874; f) A. Guéguen, D. Streich, M. He, M. Mendez, F. F. Chesneau, P. Novák, E. J. Berg, *J. Electrochem. Soc.* **2016**, *163*, A1095–A1100; g) L. Boulet-Roblin, M. E. Kazzi, P. Novak, C. Villevieille, *J. Electrochem. Soc.* **2015**, *162*, A1297–A1300; h) B. Strehle, K. Kleiner, R. Jung, F. Chesneau, M. Mendez, H. A. Gasteiger, M. Piana, *J. Electrochem. Soc.* **2017**, *164*, A400–A406; i) D. Streich, A. Guéguen, M. Mendez, F. Chesneau, P. Novák, E. J. Berg, *J. Electrochem. Soc.* **2016**, *163*, A964–A970; j) C. Villevieille, P. Lanz, C. Bünzli, P. Novák, *J. Mater. Chem. A* **2014**, *2*, 6488; k) M. M. Thackeray, C. S. Johnson, J. T. Vaughey, N. Li, S. A. Hackney, *J. Mater. Chem.* **2005**, *15*, 2257; l) E. J. Berg, C. Villevieille, D. Streich, S. Trabesinger, P. Novák, *J. Electrochem. Soc.* **2015**, *162*, A2468–A2475; m) J. Yan, X. Liu, B. Li, *RSC Adv.* **2014**, *4*, 63268.

[7] S. Zhou, G. Wang, W. Tang, Y. Xiao, K. Yan, *Solid-State Electron.* **2018**, *261*, 565.

[8] J. Yang, Y. Xia, *J. Electrochem. Soc.* **2016**, *163*, A2665–A2672.

[9] H.-J. Noh, S. Youn, C. S. Yoon, Y.-K. Sun, *J. Power Sources* **2013**, *233*, 121.

[10] J. Li, L. E. Downie, L. Ma, W. Qiu, J. R. Dahn, *J. Electrochem. Soc.* **2015**, *162*, A1401–A1408.

[11] L. de Biasi, A. O. Kondrakov, H. Geßwein, T. Brezesinski, P. Hartmann, J. Janek, *J. Phys. Chem. C* **2017**, *121*, 26163.

[12] J. Zheng, W. H. Kan, A. Manthiram, *ACS Appl. Mater. Interfaces* **2015**, *7*, 6926.

[13] S.-U. Woo, B.-C. Park, C. S. Yoon, S.-T. Myung, J. Prakash, Y.-K. Sun, *J. Electrochem. Soc.* **2007**, *154*, A649.

[14] W. Liu, P. Oh, X. Liu, M.-J. Lee, W. Cho, S. Chae, Y. Kim, J. Cho, *Angew. Chem. Int. Ed.* **2015**, *54*, 4440.

[15] J. Wang, C. Du, C. Yan, X. Xu, X. He, G. Yin, P. Zuo, X. Cheng, Y. Ma, Y. Gao, *RSC Adv.* **2016**, *6*, 26307.

[16] a) X. Xiong, Z. Wang, X. Yin, H. Guo, X. Li, *Mater. Lett.* **2013**, *110*, 4; b) S. Solchenbach, G. Hong, A. T. S. Freiberg, R. Jung, H. A. Gasteiger, *J. Electrochem. Soc.* **2018**, *165*, A3304–A3312.

[17] R. Jung, F. Linsenmann, R. Thomas, J. Wandt, S. Solchenbach, F. Maglia, C. Stinner, M. Tromp, H. A. Gasteiger, *J. Electrochem. Soc.* **2019**, *166*, A378–A389.

[18] H.-H. Sun, A. Manthiram, *Chem. Mater.* **2017**, *29*, 8486.

[19] R. Jung, R. Morasch, P. Karayaylali, K. Phillips, F. Maglia, C. Stinner, Y. Shao-Horn, H. A. Gasteiger, *J. Electrochem. Soc.* **2018**, *165*, A132–A141.

[20] J. Paulsen, J. H. Kim, US2014/0054495A1.

[21] Z. Chen, J. Wang, J. Huang, T. Fu, G. Sun, S. Lai, R. Zhou, K. Li, J. Zhao, *J. Power Sources* **2017**, *363*, 168.

[22] a) N. V. Faenza, L. Bruce, Z. W. Lebens-Higgins, I. Plitz, N. Pereira, L. F. J. Piper, G. G. Amatucci, *J. Electrochem. Soc.* **2017**, *164*, A3727–A3741; b) H. S. Liu, Z. R. Zhang, Z. L. Gong, Y. Yang, *Electrochem. Solid-State Lett.* **2004**, *7*, A190; c) I. A. Shkrob, J. A. Gilbert, P. J. Phillips, R. Klie, R. T. Haasch, D. Bareño, D. P. Abraham, *J. Electrochem. Soc.* **2017**, *164*, A1489–A1498.

[23] K. Matsumoto, R. Kuzuo, K. Takeya, A. Yamanaka, *J. Power Sources* **1999**, *81–82*, 558.

[24] K. Shizuka, C. Kiyohara, K. Shima, Y. Takeda, *J. Power Sources* **2007**, *166*, 233.

[25] J. Sicklinger, M. Metzger, H. Beyer, D. Pritzl, H. A. Gasteiger, *J. Electrochem. Soc.* **2019**, *166*, A2322–A2335.

[26] H. Wang, W. Ge, W. Li, F. Wang, W. Liu, M.-Z. Qu, G. Peng, *ACS Appl. Mater. Interfaces* **2016**, *8*, 18439.

[27] S.-W. Lee, M.-S. Kim, J. H. Jeong, D.-H. Kim, K. Y. Chung, K. C. Roh, K.-B. Kim, *J. Power Sources* **2017**, *360*, 206.

[28] a) Y.-Y. Sun, S. Liu, Y.-K. Hou, G.-R. Li, X.-P. Gao, *J. Power Sources* **2019**, *410–411*, 115; b) J. Wang, C. Du, C. Yan, X. He, B. Song, G. Yin, P. Zuo, X. Cheng, *Solid-State Electron.* **2015**, *174*, 1185; c) K. S. Yoo, Y. H. Kang, K. R. Im, C.-S. Kim, *Materials* **2017**, *10*.

[29] K. Min, K. Park, S. Y. Park, S.-W. Seo, B. Choi, E. Cho, *J. Electrochem. Soc.* **2018**, *165*, A79–A85.

[30] a) H. Gao, X. Zeng, Y. Hu, V. Tileli, L. Li, Y. Ren, X. Meng, F. Maglia, P. Lamp, S.-J. Kim, et al., *ACS Appl. Mater. Interfaces* **2018**, *1*, 2254; b) C. Qin, J. Cao, J. Chen, G. Dai, T. Wu, Y. Chen, Y. Tang, A. Li, Y. Chen, *Dalton Trans.* **2016**, *45*, 9669.

[31] F. Schipper, H. Bouzaglo, M. Dixit, E. M. Erickson, T. Weigel, M. Talianker, J. Grinblat, L. Burstein, M. Schmidt, J. Lampert, et al., *Adv. Energy Mater.* **2018**, *8*, 1701682.

[32] D. Aurbach, O. Srur-Lavi, C. Ghanty, M. Dixit, O. Haik, M. Talianker, Y. Grinblat, N. Leifer, R. Lavi, D. T. Major, et al., *J. Electrochem. Soc.* **2015**, *162*, A1014–A1027.

[33] H.-H. Sun, J.-Y. Hwang, C. S. Yoon, A. Heller, C. B. Mullins, *ACS Nano* **2018**.

[34] Q. Ran, H. Zhao, Y. Hu, Q. Shen, W. Liu, J. Liu, X. Shu, M. Zhang, S. Liu, M. Tan, et al., *Solid-State Electron.* **2018**, *289*, 82.

[35] B.-J. Chae, T. Yim, *Mater. Chem. Phys.* **2018**, *214*, 66.

[36] H. Dong, G. Liu, S. Li, S. Deng, Y. Cui, H. Liu, H. Liu, X. Sun, *ACS Appl. Mater. Interfaces* **2018**.

[37] a) Y. Zhang, Z.-B. Wang, F.-D. Yu, L.-F. Que, M.-J. Wang, Y.-F. Xia, Y. Xue, J. Wu, *J. Power Sources* **2017**, *358*, 1; b) O. Breuer, A. Chakraborty, J. Liu, T. Kravchuk, L. Burstein, J. Grinblat, Y. Kauffman, A. Gladkih, P. Nayak, M. Tsubery, et al., *ACS Appl. Mater. Interfaces* **2018**, *10*, 29608; c) B. Pişkin, C. Savaş Uygur, M. K. Aydınol, *Int. J. Energy Res.* **2018**, *42*, 3888.

[38] M. Dixit, B. Markovsky, D. Aurbach, D. T. Major, *J. Electrochem. Soc.* **2017**, *164*, A6359–A6365.

[39] M. Eilers-Rethwisch, M. Winter, F. M. Schappacher, *J. Power Sources* **2018**, *387*, 101.

[40] a) M. Eilers-Rethwisch, S. Hildebrand, M. Evertz, L. Ibing, T. Dagger, M. Winter, F. M. Schappacher, *J. Power Sources* **2018**, *397*, 68; b) G. Kang, K. Lee, K. Kwon, J. Song, *Metals* **2017**, *7*, 395.

[41] L. Liu, J. Li, Y. Xiao, W. Sun, B. Yue, *J. Mater. Sci. Mater. Electron.* **2018**, *29*, 21213.

[42] a) B. Han, S. Xu, S. Zhao, G. Lin, Y. Feng, L. Chen, D. G. Ivey, P. Wang, W. Wei, *ACS Appl. Mater. Interfaces* **2018**, *10*, 39599; b) X. Li, K. Zhang, M. Wang, Y. Liu, M. Qu, W. Zhao, J. Zheng, *Sustain. Energy Fuels* **2018**, *2*, 413.

[43] R. Zhao, J. Liang, J. Huang, R. Zeng, J. Zhang, H. Chen, G. Shi, *J. Alloys Compd.* **2017**, *724*, 1109.

[44] U. Breddemann, I. Krossing, *ChemElectroChem* **2020**, *7*, 1389.

[45] P. Yue, Z. Wang, H. Guo, X. Xiong, X. Li, *Solid-State Electron.* **2013**, *92*, 1.

[46] P. Yue, Z. Wang, J. Wang, H. Guo, X. Xiong, X. Li, *Powder Technol.* **2013**, *237*, 623.

[47] M. Ménétrier, J. Bains, L. Croguennec, A. Flambard, E. Bekaert, C. Jordy, P. Biensan, C. Delmas, *J. Solid State Chem.* **2008**, *181*, 3303.

[48] L. Croguennec, J. Bains, M. Ménétrier, A. Flambard, E. Bekaert, C. Jordy, P. Biensan, C. Delmas, *J. Electrochem. Soc.* **2009**, *156*, A349.

[49] L. Li, B. H. Song, Y. L. Chang, H. Xia, J. R. Yang, K. S. Lee, L. Lu, *J. Power Sources* **2015**, *283*, 162.

[50] U. Breddemann, E. M. Erickson, V. Davis, F. Schipper, M. Ellwanger, M. Daub, A. Hoffmann, C. Erk, B. Markovsky, D. Aurbach, et al., *ChemElectroChem* **2019**.

[51] a) E. M. Erickson, H. Sclar, F. Schipper, J. Liu, R. Tian, C. Ghanty, L. Burstein, N. Leifer, J. Grinblat, M. Talianker, et al., *Adv. Energy Mater.* **2017**, *26*, 1700708; b) E. M. Erickson, F. Schipper, R. Tian, J.-Y. Shin, C. Erk, F. F. Chesneau, J. K. Lampert, B. Markovsky, D. Aurbach, *RSC Adv.* **2017**, *7*, 7116; c) F. Amalraj, M. Talianker, B. Markovsky, L. Burlaka, N. Leifer, G. Goobes, E. M. Erickson, O. Haik, J. Grinblat, E. Zinigrad, et al., *J. Electrochem. Soc.* **2013**, *160*, A2220–A2233.

[52] D. R. Lide (Ed.) *CRC handbook of chemistry and physics. A ready-reference book of chemical and physical data*, CRC Press, Boca Raton, Fla., **1997**.

[53] K. Nakamoto, *Infrared and Raman spectra of inorganic and coordination compounds. Part A: Theory and applications in inorganic chemistry*, Wiley, Hoboken, N.J, **2009**.

[54] N. Dupre, M. Cuisinier, D. Guyomard, *Interface* **2011**, *20*, 61.

[55] E. Boivin, R. David, J.-N. Chotard, T. Bamine, A. Iadecola, L. Bourgeois, E. Suard, F. Fauth, D. Carlier, C. Masquelier, et al., *Chem. Mater.* **2018**.

[56] S. Zhong, L. Liu, J. Liu, J. Wang, J. Yang, *Solid State Commun.* **2009**, *149*, 1679.

[57] Y. Zhang, Q. Liang, C. Huang, P. Gao, H. Shu, X. Zhang, X. Yang, L. Liu, X. Wang, *Solid-State Electron.* **2018**, *22*, 1995.

[58] P. F. Xiao, M. O. Lai, L. Lu, *Solid State Ionics* **2013**, *242*, 10.

[59] D. Chen, G.-Q. Shao, B. Li, G.-G. Zhao, J. Li, J.-H. Liu, Z.-S. Gao, H.-F. Zhang, *Solid-State Electron.* **2014**, *147*, 663.

[60] a) D. R. Gallus, R. Schmitz, R. Wagner, B. Hoffmann, S. Nowak, I. Cekic-Laskovic, R. W. Schmitz, M. Winter, *Electrochim. Acta* **2014**, *134*, 393; b) H. Zheng, Q. Sun, G. Liu, X. Song, V. S. Battaglia, *J. Power Sources* **2012**, *207*, 134.

[61] S. Yonezawa, M. Yamasaki, M. Takashima, *J. Fluorine Chem.* **2004**, *125*, 1657.

[62] M. Ueda, M. Ohe, J.-H. Kim, S. Yonezawa, M. Takashima, *J. Fluorine Chem.* **2013**, *149*, 88.

[63] A. Chakraborty, S. Kunnikuruvan, M. Dixit, D. T. Major, *Isr. J. Chem.* **2020**, *25*, 71.

[64] a) Y. W. Tsai, B. J. Hwang, G. Ceder, H. S. Sheu, D. G. Liu, J. F. Lee, *Chem. Mater.* **2005**, *17*, 3191; b) W.-S. Yoon, M. Balasubramanian, K. Y. Chung, X.-Q. Yang, J. McBreen, C. P. Grey, D. A. Fischer, *J. Am. Chem. Soc.* **2005**, *127*, 17479; c) M. Dixit, B. Markovsky, F. Schipper, D. Aurbach, D. T. Major, *J. Phys. Chem. C* **2017**, *121*, 22628.

[65] a) J.-M. Kim, H.-T. Chung, *Solid-State Electron.* **2004**, *49*, 937; b) Y. Koyama, I. Tanaka, H. Adachi, Y. Makimura, T. Ohzuku, *J. Power Sources* **2003**, *119–121*, 644; c) B. J. Hwang, Y. W. Tsai, D. Carlier, G. Ceder, *Chem. Mater.* **2003**, *15*, 3676; d) A. Deb, U. Bergmann, S. P. Cramer, E. J. Cairns, *J. Electrochem. Soc.* **2005**, *97*, 113523; e) M. Dixit, M. Kosa, O. S. Lavi, B. Markovsky, D. Aurbach, D. T. Major, *Phys. Chem. Chem. Phys.* **2016**, *18*, 6799; f) K.-W. Nam, S.-M. Bak, E. Hu, X. Yu, Y. Zhou, X. Wang, L. Wu, Y. Zhu, K.-Y. Chung, X.-Q. Yang, *Adv. Funct. Mater.* **2013**, *23*, 1047.

[66] Y. Shao-Horn, L. Croguennec, C. Delmas, E. C. Nelson, M. A. O'Keefe, *Nat. Mater.* **2003**, *2*, 464.

[67] a) W. Xu, *Int. J. Electrochem. Sci.* **2017**, 9758; b) J. Lu, K. S. Lee, *Mater. Technol.* **2016**, *31*, 628.

[68] J.-H. Cheng, C.-J. Pan, J.-F. Lee, J.-M. Chen, M. Guignard, C. Delmas, D. Carlier, B.-J. Hwang, *Chem. Mater.* **2014**, *26*, 1219.

[69] D. Petzold, *J. Therm. Anal.* **1985**, *30*, 391.

[70] V. Pralong, A. Delahaye-Vidal, B. Beaudoin, B. Gérand, J.-M. Tarascon, *J. Mater. Chem.* **1999**, *9*, 955.